Article

Unconventional ferroelectricity in moiré heterostructures

https://doi.org/10.1038/s41586-020-2970-9

Received: 6 May 2020

Accepted: 7 October 2020

Published online: 23 November 2020

Check for updates

Zhiren Zheng[1,9], Qiong Ma[1,2,9]✉, Zhen Bi[1], Sergio de la Barrera[1], Ming-Hao Liu[3], Nannan Mao[4,5], Yang Zhang[1], Natasha Kiper[1], Kenji Watanabe[6], Takashi Taniguchi[7], Jing Kong[4], William A. Tisdale[5], Ray Ashoori[1], Nuh Gedik[1], Liang Fu[1], Su-Yang Xu[1,8] & Pablo Jarillo-Herrero[1]✉

The constituent particles of matter can arrange themselves in various ways, giving rise to emergent phenomena that can be surprisingly rich and often cannot be understood by studying only the individual constituents. Discovering and understanding the emergence of such phenomena in quantum materials—especially those in which multiple degrees of freedom or energy scales are delicately balanced—is of fundamental interest to condensed-matter research[1,2]. Here we report on the surprising observation of emergent ferroelectricity in graphene-based moiré heterostructures. Ferroelectric materials show electrically switchable electric dipoles, which are usually formed by spatial separation between the average centres of positive and negative charge within the unit cell. On this basis, it is difficult to imagine graphene—a material composed of only carbon atoms—exhibiting ferroelectricity[3]. However, in this work we realize switchable ferroelectricity in Bernal-stacked bilayer graphene sandwiched between two hexagonal boron nitride layers. By introducing a moiré superlattice potential (via aligning bilayer graphene with the top and/or bottom boron nitride crystals), we observe prominent and robust hysteretic behaviour of the graphene resistance with an externally applied out-of-plane displacement field. Our systematic transport measurements reveal a rich and striking response as a function of displacement field and electron filling, and beyond the framework of conventional ferroelectrics. We further directly probe the ferroelectric polarization through a non-local monolayer graphene sensor. Our results suggest an unconventional, odd-parity electronic ordering in the bilayer graphene/boron nitride moiré system. This emergent moiré ferroelectricity may enable ultrafast, programmable and atomically thin carbon-based memory devices.

Discovering and classifying novel phases of matter has been a constant driving force throughout condensed-matter research. For example, the recognition of spontaneous symmetry breaking has enabled the study and understanding of superconductors, magnets and many other correlated electronic states under a unifying principle. The concepts of Berry phase and topology have led to novel topological phases, including quantum spin Hall insulators, three-dimensional topological insulators and Weyl semimetals[4]. With these exciting advances, it is increasingly recognized that one of the next frontiers to discover new physics lies in systems where electronic correlations, spontaneous symmetry breaking and Berry phase are all at play[1,2]. The realization of such systems with a variety of degrees of freedom in a delicate balance calls for unprecedented ability to design, engineer and control the electronic and symmetry properties of quantum materials.

In that sense, two-dimensional (2D) moiré superlattices offer a uniquely suitable platform because they allow for a powerful, yet generic, way to induce electronic correlations into systems where interactions are otherwise not strong. For instance, monolayer graphene is a weakly interacting 2D semimetal. However, stacking one monolayer of graphene on another at the magic angle (around 1.1°) strongly modifies the electronic structure[5–7], giving rise to emergent phenomena[8,9]. Current research, which has included a number of different moiré superlattices[10–21], has uncovered superconducting and magnetic states, among others. Superconductivity and magnetism correspond to the spontaneous breaking of gauge symmetry (charge conservation) and spin rotational symmetry, respectively. Another class of symmetry that plays an important role in both correlated physics and topology is the point group symmetries, such as inversion, mirror reflection and rotation. The spontaneous breaking of point group symmetries can give rise to a wide range of novel electronic orders[22–25]. Moreover, these electronic orders are predicted to serve as precursors to unconventional superconducting pairing[26] or novel magnetism[27].

[1]Department of Physics, Massachusetts Institute of Technology, Cambridge, MA, USA. [2]Department of Physics, Boston College, Chestnut Hill, MA, USA. [3]Department of Physics, National Cheng Kung University, Tainan, Taiwan. [4]Department of Electrical Engineering and Computer Science, Massachusetts Institute of Technology, Cambridge, MA, USA. [5]Department of Chemical Engineering, Massachusetts Institute of Technology, Cambridge, MA, USA. [6]Research Center for Functional Materials, National Institute for Materials Science, Tsukuba, Japan. [7]International Center for Material Nanoarchitectonics, National Institute for Materials Science, Tsukuba, Japan. [8]Department of Chemistry and Chemical Biology, Harvard University, Cambridge, MA, USA. [9]These authors contributed equally: Zhiren Zheng, Qiong Ma. ✉e-mail: qiongm@mit.edu; pjarillo@mit.edu

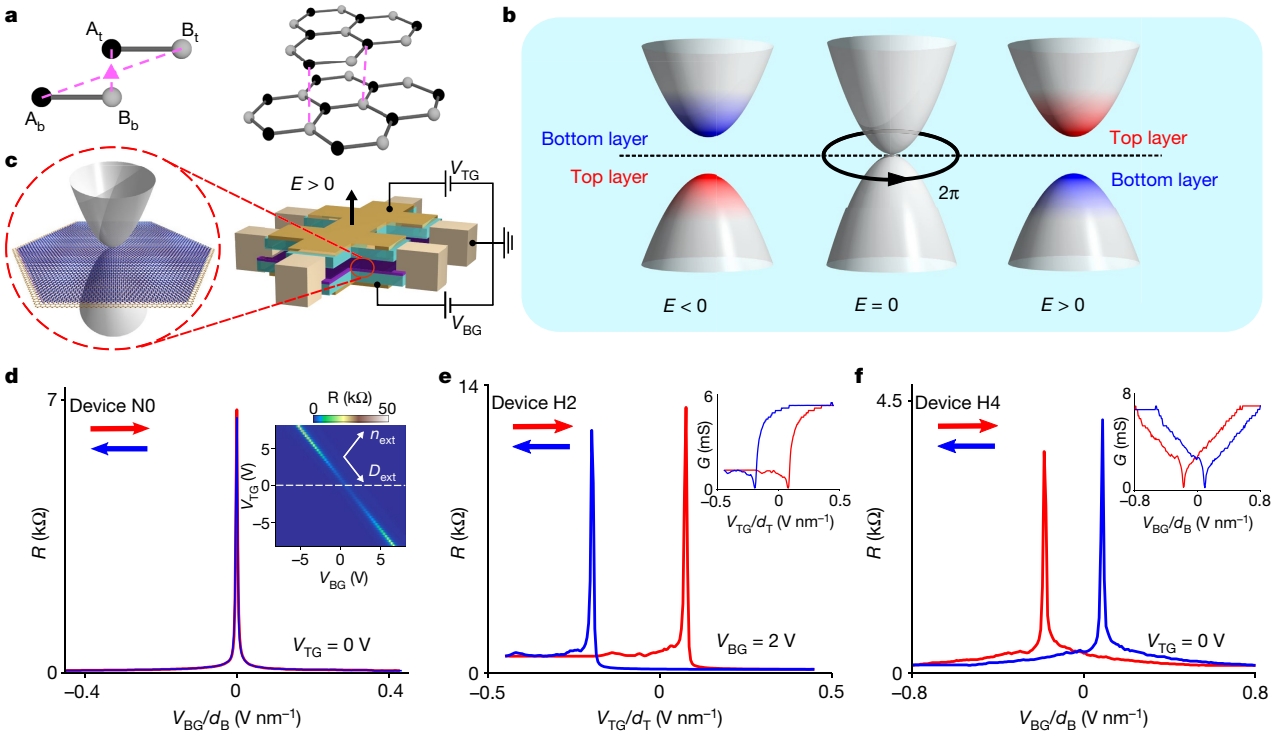

Fig. 1 | Quadratic, chiral fermions on a moiré potential in a BLG/BN moiré superlattice. a, Lattice structure of Bernal-stacked BLG. The triangle marks its inversion centre. $A_{t(b)}$ and $B_{t(b)}$ are the A and B sublattices on the top (bottom) layer, which forms two inversion pairs, (A_t, B_b) and (A_b, B_t), connected by dashed lines. **b**, Schematic of the band dispersion and layer polarization of the low-energy electronic states of pristine BLG at different interlayer electric fields. **c**, Schematic of our BN-encapsulated bilayer device with top (V_{TG}) and bottom (V_{BG}) gates. The black arrow identifies the positive electric-field direction. Left: schematic of the BLG/BN moiré superlattice pattern. One-side alignment is shown with an enlarged lattice mismatch for clarity. **d**–**f**, Four-probe resistance for a normal BLG device N0 (**d**) and the hysteretic devices H2 (**e**) and H4 (**f**). The x axis V_{BG} (V_{TG}) is normalized by the bottom BN thickness d_B (d_T). The forward and backward scans are shown in red and blue, respectively. The inset in **d** is the dual-gate map of the four-probe resistance for the normal BLG. The insets in **e** and **f** are the conductance (G) plots.

However, apart from a few studies reporting evidence of nematicity in magic-angle graphene[28–30] and the observation of the quantum anomalous Hall effect in boron nitride (BN)-aligned magic-angle and ABC graphene[11,12,14,31], the role of point group symmetries in moiré systems remains largely under-explored.

Here we study Bernal-stacked bilayer graphene (BLG)[32] aligned with BN, a simple yet rich moiré system where electronic correlations, Berry phase and point group symmetries (such as inversion symmetry) are simultaneously important. In Bernal-stacked BLG, the unit cell consists of two inversion pairs (Fig. 1a). The space inversion symmetry is effectively equivalent to the layer degeneracy. The application of an external out-of-plane displacement field breaks the layer degeneracy and gives rise to a layer polarization in the quantum wavefunction near the band edges, and hence a non-zero Berry curvature (Fig. 1b). Such Berry curvature lies at the heart of the topological valley transport as well as chiral optical and excitonic properties in BLG[33–37]. Owing to this unique electronic structure, theory has long predicted a wide range of spontaneous electronic order in pristine BLG[32]. Under high magnetic fields at very low temperatures, experiments have indeed revealed a number of broken symmetry phases in the Landau levels[38,39]. In contrast, in the absence of a magnetic field, interesting experimental results have suggested electronic correlations[40–43], but the effects remain relatively subtle even at very low temperatures with ultrahigh-quality samples, and their exact nature remains unsettled. Here we put such chiral, quadratic gapless fermions that are protected by the layer degeneracy onto a moiré superlattice potential (Fig. 1c), to search for correlation-driven spontaneous symmetry breaking. In the following, we report on the observation of emergent unconventional ferroelectricity in this system.

We have fabricated high-quality, BN-encapsulated, dual-gated BLG devices, as shown in Fig. 1c. This allows us to independently tune the externally applied charge density, n_{ext}, and the out-of-plane electric displacement field, D_{ext}, through experimental control of the gate voltages (Methods). The moiré superlattice potential is introduced by the rotational alignment between the BLG and the encapsulating BN flakes, which plays a crucial role in the observed ferroelectricity. Such rotational alignment was achieved by aligning the straight edges of the BLG flake and one of the BN flakes. The other degree of freedom is the relative angle between the top and bottom BN flakes. In devices H2 and H4, the top and bottom BN flakes have a relative angle of about 30° and about 0°, respectively; in devices H1 and H3, the top and bottom BN flakes have a relative angle of about 20° (Methods). Devices H2 and H4 show dramatic hysteretic responses to the externally applied displacement field, whereas the hysteresis in devices H1 and H3 is relatively weaker.

Ferroelectric response in the BLG/BN moiré system

In the main text, we focus on the hysteretic characteristics of devices H2 and H4. All the data shown were taken at temperature $T = 4$ K, unless otherwise noted. In Fig. 1d, the normal BLG (device N0) shows no hysteresis between the forward and backward bottom gate voltage, V_{BG}, scans, whereas devices H2 and H4 (Fig. 1e, f) show substantial hysteresis. It is interesting to note that the resistance hysteresis loops for devices H2 and H4 have the opposite sequence in terms of whether the resistance peak appears in an advanced or a retarded fashion, pointing to the unconventional nature of the ferroelectricity (Supplementary Section III).

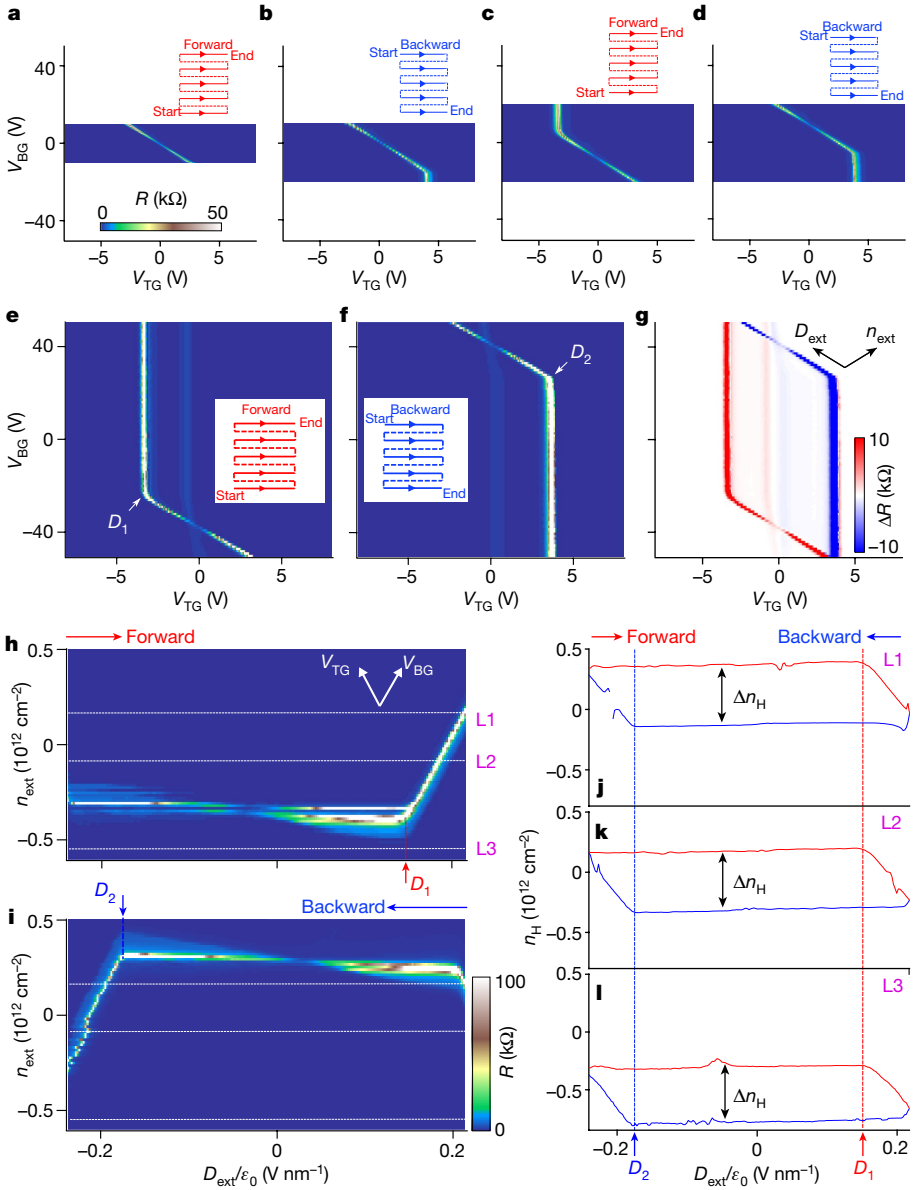

Fig. 2 | Hysteretic transport behaviour for device H4. a–**d**, The four-probe longitudinal resistance as a function of the top gate voltage, V_{TG}, and the bottom gate voltage, V_{BG} with range from −10 V to 10 V (**a**), from 10 V to −20 V (**b**), from −20 V to 20 V (**c**), and from 20 V to −20 V (**d**). Insets: the 'zigzag' patterns illustrate how the data are taken. 'Start' ('End') denotes the starting (ending) point for each dual-gate map. During these measurements, V_{TG} is swept as the fast-scan axis and V_{BG} is swept as the slow-scan axis. At a fixed V_{BG}, we scan V_{TG} from −8 V to +8 V while recording data (solid lines) and then ramp back to −8 V continuously without recording (dashed lines). We change V_{BG} by a small step and scan V_{TG} back and forth again. Only the data collected along the solid lines are shown. **e**, **f**, Forward (**e**) and backward (**f**) scans for V_{BG} swept between −50 V and 50 V. **g**, The difference between resistance measured in **e** and **f**. **h**, **i**, The resistance measured while sweeping the externally applied displacement field D_{ext} in the forward (**h**) and backward (**i**) directions at each fixed carrier density n_{ext}. The carrier density scan direction is from the negative to positive values. **j**–**l**, Carrier density (n_H) extracted from Hall measurements along the lines L1 (**j**), L2 (**k**) and L3 (**l**) denoted in **h** and **i**.

To further illustrate this behaviour, we now systematically show the hysteretic transport behaviour of device H4 by presenting the four-probe resistance measured as a function of top and bottom gate voltages (V_{TG} and V_{BG}). (1) In the range of V_{TG} from −8 V to +8 V and V_{BG} from −10 V to +10 V (Fig. 2a), device H4 behaves almost like normal BLG with the gapless point at $V_{TG} = V_{BG} = 0$. (2) We reverse the scan direction of V_{BG} and scan V_{BG} from +10 V to −10 V. Identical normal BLG behaviour is observed. (3) However, when we further extend the range of V_{BG} downward (Fig. 2b), the resistance peak ridge suddenly turns to be almost parallel to the V_{BG} axis on reaching $V_{BG} \approx -15$ V. In other words, in this regime, the device appears to behave as though the bottom gate 'stops working', whereas the top gate still functions normally. In the following, we refer to such a phenomenon as 'layer-specific anomalous screening' (LSAS) because the phenomenon suggests that the electric field from a specific gate appears to be anomalously screened (Supplementary Section III). (4) On reaching $V_{BG} = -20$ V, we reverse again the scanning direction of V_{BG} (Fig. 2c). Equally strikingly, the LSAS behaviour immediately stops and normal BLG behaviour is recovered. (5) However, once we reach far enough on the opposite side of the gapless point, we enter another LSAS regime (Fig. 2c). (6) At this point, if we reverse the scanning direction of V_{BG} again, the resistance immediately follows a normal BLG behaviour and switches to the LSAS behaviour after a certain distance across the gapless point (Fig. 2d). As such, the resistance peak lines for the two scanning directions form

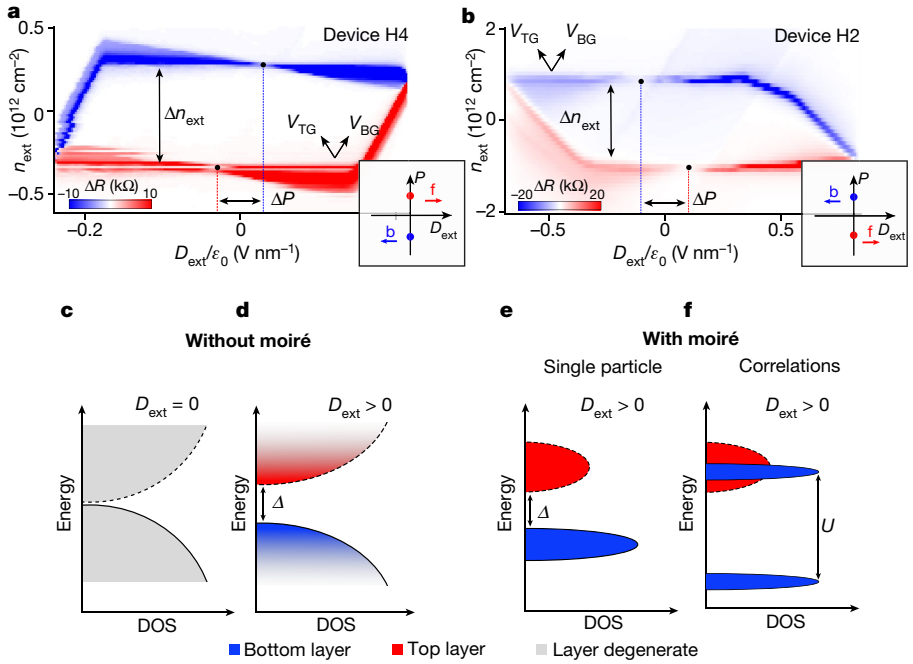

Fig. 3 | Measuring the out-of-plane electric polarization and a possible microscopic picture based on interlayer charge transfer. a, The resistance difference between Fig. 2h and Fig. 2i for device H4. $\Delta P_{H4} = P_{forward} - P_{backward} = +0.05\,\mu C\,cm^{-2}$. **b**, Same as **a** but for device H2. $\Delta P_{H2} = P_{forward} - P_{backward} = -0.18\,\mu C\,cm^{-2}$. Insets: The remnant polarization in the forward (f) and backward (b) scans. **c**–**f**, Schematics of energy versus density of states (DOS) under four scenarios: pristine BLG without a moiré superlattice at zero external displacement field (**c**) and at positive external displacement field (**d**) and device H4 at positive external displacement field in a single particle picture (**e**) and with consideration of correlation effect (**f**).

a parallelogram (Fig. 2e–g, Extended Data Fig. 2). In other words, we observe very prominent hysteretic behaviour depending on the bottom gate scanning direction. However, no anomalous screening is observed along the top gate direction (Supplementary Section V.3). A complete set of equivalent measurements for device H2 is shown in Extended Data Figs. 3, 4, with similarly dramatic hysteretic characteristics.

We summarize a few key observations in Fig. 2a–g. (1) Two particular electric displacement fields on opposite sides of the gapless point (D_1 and D_2 in Fig. 2e, f) separate the normal BLG behaviour region and the LSAS region. When scanning upward with increasing V_{BG}, the peak line becomes parallel to the V_{BG} axis on reaching D_1 (Fig. 2e). The same applies for D_2 when scanning downward with decreasing V_{BG} (Fig. 2f). Similar behaviour is observed when the bottom gate is used as the fast-scan axis (Supplementary Section V.3). (2) Interestingly, D_1 and D_2 appear to be fixed with respect to the gapless point, whose position in the parameter space of (V_{TG}, V_{BG}) can vary depending on the scanning history (Extended Data Fig. 2).

Hall measurement along D_{ext}

We now change the scan variables to D_{ext} (fast axis) and n_{ext} (slow axis) by sweeping V_{TG} and V_{BG} simultaneously. Consistent results are observed, as shown in Fig. 2h, i. The transverse resistance R_{xy} directly measures the (mobile) charge density $n_H = B/(eR_{xy})$ (where B is the perpendicular magnetic field and e is the electron charge), which therefore allows us to probe the conductive regimes that appear less prominent in the resistance maps. In Fig. 2j, for the forward scan (red curve), n_H shows that the system is electron doped, and the mobile charge density remains roughly unchanged for $D_{ext} < D_1$. However, for $D_{ext} > D_1$, n_H starts to deviate, consistent with the LSAS observed in resistance, and, as a result, D_{ext} can change the mobile charge density of the system. We now reverse D_{ext} to scan backward. As described above, the moment we reverse the scan direction, the LSAS behaviour stops, so n_H (blue curve) maintains a constant value until we reach D_2. We show n_H at three fixed n_{ext} values (Fig. 2j–l). Interestingly, n_H always starts to change at the same D_{ext} values and with the same Δn_H. Therefore, our Hall measurements show that D_1 and D_2 are the same irrespective of n_{ext} within our accessible scan range. Similar Hall measurements were also conducted in device H2, as shown in Extended Data Fig. 5. We note that both the LSAS behaviour and the ability of D_{ext} to change the mobile charge density are very surprising and not observed in other two-dimensional systems. We will return to this point in the latter part of the paper.

Measurement of remnant polarization

We now show how the hysteretic resistance map in the (D_{ext}, n_{ext}) parameter space can be used to visualize and to measure a switchable out-of-plane spontaneous polarization, that is, ferroelectric ordering. Unique to bilayer graphene, the gapless band touching is only realized when the top and bottom layers are degenerate, which implies an absence of an electrical displacement field across the two layers. In the presence of ferroelectric ordering, the interlayer displacement field has two contributions, the field induced by gating (roughly D_{ext}) and the internal electric field arising from the built-in ferroelectric polarization (P). As such, the gapless point is only realized when the externally induced and internal fields cancel each other out, that is, zero total interlayer displacement field (see Supplementary Section IV for further discussion). As shown in Fig. 3a, the gapless points that appear in the two normal bilayer regimes (horizontal resistance peak lines) are located at non-zero and opposite D_{ext} values, demonstrating the existence of a switchable, remnant polarization. From this analysis, we can directly read out $\Delta D_{ext}/\varepsilon_0$ (where ε_0 is the vacuum permittivity) from Fig. 3a and convert into the remnant polarization by simply multiplying ε_0. For device H4, $\Delta P_{H4} = P_{forward} - P_{backward} = +0.05\,\mu C\,cm^{-2}$. Interestingly, the remnant polarization scales with the range of the displacement field, which is further explored in Supplementary Section V.3. In addition, we probe the polarization of device H4 independently by a non-local monolayer graphene sensor, a technique recently

demonstrated in ref. [44], and we obtain consistent results (Methods). Similarly, device H2 also shows prominent hysteresis that forms a parallelogram (Fig. 3b). In device H2, it is the top gate that appears to be 'not working' in the switching regime, which is manifested as the opposite tilting direction of the parallelogram in Fig. 3b (see more data on device H2 in Supplementary Section V.2). Using the same method, we obtain $\Delta P_{H2} = P_{forward} - P_{backward} = -0.18\ \mu C\ cm^{-2}$ for device H2. Intriguingly, device H4 and device H2 have opposite remnant electrical polarization (insets of Fig. 3a, b). Consequently, the P–D_{ext} loop in device H4 is clockwise while the P–D_{ext} loop in device H2 is anticlockwise as a result of their opposite sequence between the normal BLG and LSAS behaviour (Supplementary Section III). In fact, the opposite behaviours have already been suggested by the opposite sequences of the resistance switching shown in Fig. 1e, f. A conventional ferroelectric material has an anticlockwise P–E loop (where E is the electric field). Therefore, in this sense, the behaviour of device H4 is highly unusual. Moreover, here we observe both opposite behaviours in devices H4 and H2. We provide a possible microscopic picture below.

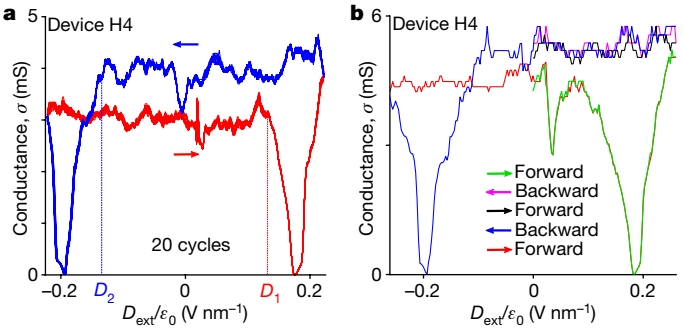

Fig. 4 | Robustness of the ferroelectric switching in the graphene/BN moiré system. a, Measurements of the conductance at $n_{ext} = 0$ for forward and backward sweeps of D_{ext} (repeated 20 times). **b**, Consecutive measurements of conductance as a function of D_{ext} with alternating forward and backward scan directions (denoted by the coloured arrows) and for different scan ranges.

A microscopic theoretical picture

Our observation of strong hysteresis and LSAS phenomena provide an incentive to understand the underlying mechanism. Our systematic measurements and analyses of the hysteretic and control devices strongly suggest that an extrinsic charge-trapping mechanism is unlikely to be responsible, and, in addition, the ferroelectric behaviour cannot be well explained based on a lattice model in the framework of conventional ferroelectrics (Methods). Instead, our theoretical analyses and experimental observations indicate an intrinsic origin and an unconventional nature of the reported ferroelectricity.

We now provide an intuitive theoretical picture based on interaction-induced interlayer charge transfer, which captures the dominant features in our data[45]. We note, however, that further theoretical work will be required to confirm the plausibility of this picture. First, we highlight important properties of the single-particle electronic structure of the BLG/BN moiré system. As mentioned above, normal BLG (misaligned to BN) has a quadratic band dispersion. An external displacement field opens a gap at the quadratic band touching and flattens the dispersion near the gap edge. Importantly, while states in the vicinity of the gap edge become layer polarized, states away from it remain layer degenerate (Fig. 3c, d). In the case of BLG aligned to BN, because of the small moiré wavevector k_m, it is possible for the entire low-energy moiré band to become highly layer polarized (Fig. 3e) at a large enough displacement field. In real space, this means that electrons occupying a moiré band at low energy are located on a specific layer. In momentum space, this means that the low-energy moiré band will become increasingly flat. Without loss of generality, let us consider a large positive displacement field. Then the highest moiré valence band and the lowest moiré conduction band will be largely polarized to the bottom layer and top layer, respectively (Fig. 3e).

Second, we now consider the effect of correlations. As one increases the displacement field, the bands become increasingly flat and layer polarized. The kinetic energy becomes quenched, making the effect of correlations (for example, on-site Coulomb repulsion) more substantial. This gate-tunable correlation effect is a unique property of BLG, where bandgap formation through an external electric field allows modification of the bandwidth, effective mass and, hence, correlation strength (Supplementary Section IV). Based on our data, we assume that the on-site repulsion in the bottom layer is the relevant one in device H4. This layer asymmetry translates into the asymmetry between the moiré valence and conduction bands due to the electronic layer polarization. In this particular discussion ($D_{ext} > 0$), the correlation effect (on-site repulsion U) dominates in the moiré valence band. There may be a critical displacement field above which the on-site repulsion U in the bottom layer (valence band) is sufficiently strong that the moiré valence band splits into lower and upper Hubbard bands (Fig. 3f). Because U is larger than the bandgap Δ, it is energetically more favourable for electrons to occupy the moiré conduction band rather than the upper Hubbard band. This leads to a transfer of electrons from the valence band (bottom layer) to the moiré conduction band (top layer), which is accompanied by a change of the polarization. It is important to note that this polarization generated by the interlayer charge transfer is actually in the direction opposite to the externally applied positive displacement field. Further, this process is hysteretic, because increasing V_{BG} triggers the interlayer charge transfer whereas decreasing V_{BG} does not. Specifically, increasing V_{BG} adds electrons to the fully polarized upper Hubbard band (the bottom layer). This process is energetically unfavourable due to strong Coulomb repulsion. As a result, increasing V_{BG} does not introduce electrons to the graphene from the ground; rather, electrons are transferred from the bottom layer to the top layer within the graphene, leading to the observed LSAS behaviour. In contrast, decreasing V_{BG} removes electrons from the graphene system, which is energetically allowed. Therefore, when we reverse the scanning direction to decrease V_{BG}, the interlayer charge transfer does not occur; the LSAS stops and normal BLG behaviour appears. Using the fact that the interlayer charge transfer gives rise to a polarization that is in the opposite direction to the external displacement field and that the moment when we reverse the scanning direction to decrease V_{BG}, the LSAS stops and the normal BLG behaviour appears, one can find that a clockwise P–D_{ext} loop is naturally derived. This process is energetically possible due to the ability of D_{ext} to change the mobile charge density, meaning that our system is not an isolated system and it exchanges particles with the environment, unlike conventional ferroelectric materials.

With the layer-specific moiré flat bands and interlayer charge transfer picture, the ferroelectricity and LSAS behaviour in devices H4 and H2 can both be understood (Methods, Supplementary Section III). Meanwhile, it is interesting to note that a spontaneous interlayer charge transfer has been observed in the gallium arsenide double-layer system[46]. Although the above picture may capture dominant features in our data, we wish to emphasize that further experiments are needed to fully understand the observed ferroelectricity.

Robustness of the ferroelectric switching

We now present further systematic measurements to demonstrate the robustness of the ferroelectric switching. In Fig. 4a, we repeat the same hysteresis loop 20 consecutive times. All 20 scans fall exactly onto each other. Such remarkable reproducibility confirms the intrinsic nature of our observations. In Fig. 4b, we perform five consecutive D_{ext} scans along alternating forward and backward directions with

different ranges while keeping $n_{ext} = 0$. (1) We start from zero displacement field and scan D_{ext} forward (the green curve); as D_{ext} surpasses D_1, the LSAS occurs and we observe a conductance dip (resistance peak) that corresponds to cutting through the right edge of the parallelogram in Fig. 3a. (2) As soon as we turn back (pink curve), both gates function normally. Therefore, the system immediately follows a constant conductance curve. Once we reach $D_{ext} = 0$, we stop. (3) We then scan again forward (black curve). As the pink curve did not reach D_2, the black curve exactly follows the pink curve. (4) We turn around to scan backward (blue curve), this time going below D_2. As D_{ext} surpasses D_2, the system again enters the LSAS regime and we observe a resistance peak that corresponds to cutting through the left edge of the parallelogram in Fig. 3a. (5) Turning back to scan forward, both gates work normally until we reach D_1 and the behaviour is identical to the green curve. These scans confirm that the switching behaviour in device H4 is robustly triggered by reaching the LSAS regime.

Moving forward, our observations suggest many exciting possibilities. In terms of fundamental physics, it would be interesting to study many other bilayer 2D crystals under a moiré superlattice potential. In fact, the methodology applied here may be generalized to create ferroelectricity in a wide range of naturally non-polar 2D crystals. As the ferroelectric instability is intrinsically odd-parity, its introduction into magnetic or superconducting systems may induce exotic magneto-electric coupling[27] or odd-parity Cooper pairing[26]. The unconventional ferroelectricity can also enable a number of novel nonlinear optical responses. In terms of applications, by writing domains with piezoelectric force microscopy, one can design controllable topological electrical circuits[34–36]. Moreover, our systems can be used as high-performance memory devices due to the strong hysteresis, large on-off ratio and remarkable robustness. More notably, the promise of electronically driven switching may enable next-generation memory components with potentially ultrafast operation speeds.

Online content

Any methods, additional references, Nature Research reporting summaries, source data, extended data, supplementary information, acknowledgements, peer review information; details of author contributions and competing interests; and statements of data and code availability are available at https://doi.org/10.1038/s41586-020-2970-9.

1. Keimer, B. & Moore, J. E. The physics of quantum materials. *Nat. Phys.* **13**, 1045–1055 (2017).
2. Tokura, Y., Kawasaki, M. & Nagaosa, N. Emergent functions of quantum materials. *Nat. Phys.* **13**, 1056–1068 (2017).
3. Castro Neto, A. H., Guinea, F., Peres, N. M. R., Novoselov, K. S. & Geim, A. K. The electronic properties of graphene. *Rev. Mod. Phys.* **81**, 109–162 (2009).
4. Armitage, N. P., Mele, E. J. & Vishwanath, A. Weyl and Dirac semimetals in three-dimensional solids. *Rev. Mod. Phys.* **90**, 015001 (2018).
5. Suárez Morell, E., Correa, J., Vargas, P., Pacheco, M. & Barticevic, Z. Flat bands in slightly twisted bilayer graphene: tight-binding calculations. *Phys. Rev. B* **82**, 121407 (2010).
6. Li, G. et al. Observation of van Hove singularities in twisted graphene layers. *Nat. Phys.* **6**, 109–113 (2010).
7. Bistritzer, R. & MacDonald, A. H. Moiré bands in twisted double-layer graphene. *Proc. Natl Acad. Sci. USA* **108**, 12233–12237 (2011).
8. Cao, Y. et al. Unconventional superconductivity in magic-angle graphene superlattices. *Nature* **556**, 43–50 (2018).
9. Cao, Y. et al. Correlated insulator behaviour at half-filling in magic-angle graphene superlattices. *Nature* **556**, 80–84 (2018).
10. Yankowitz, M. et al. Tuning superconductivity in twisted bilayer graphene. *Science* **363**, 1059–1064 (2019).
11. Sharpe, A. L. et al. Emergent ferromagnetism near three-quarters filling in twisted bilayer graphene. *Science* **365**, 605–608 (2019).
12. Serlin, M. et al. Intrinsic quantized anomalous Hall effect in a moiré heterostructure. *Science* **367**, 900–903 (2020).
13. Chen, G. et al. Evidence of a gate-tunable Mott insulator in a trilayer graphene moiré superlattice. *Nat. Phys.* **15**, 237–241 (2019).
14. Chen, G. et al. Tunable correlated Chern insulator and ferromagnetism in a moiré superlattice. *Nature* **579**, 56–61 (2020); correction **581**, E3 (2020).
15. Burg, G. W. et al. Correlated insulating states in twisted double bilayer graphene. *Phys. Rev. Lett.* **123**, 197702 (2019).
16. Liu, X. et al. Spin-polarized correlated insulator and superconductor in twisted double bilayer graphene. *Nature* **583**, 221–225 (2020).
17. Cao, Y. et al. Tunable correlated states and spin-polarized phases in twisted bilayer–bilayer graphene. *Nature* **583**, 215–220 (2020); correction **583**, 215–220 (2020).
18. Shen, C. et al. Correlated states in twisted double bilayer graphene. *Nat. Phys.* **16**, 520–525 (2020).
19. Wang, L. et al. Correlated electronic phases in twisted bilayer transition metal dichalcogenides. *Nat. Mater.* **19**, 861–866 (2020).
20. Regan, E. C. et al. Mott and generalized Wigner crystal states in WSe_2/WS_2 moiré superlattices. *Nature* **579**, 359–363 (2020).
21. Tang, Y. et al. Simulation of Hubbard model physics in WSe_2/WS_2 moiré superlattices. *Nature* **579**, 353–358 (2020).
22. Nandkishore, R. & Levitov, L. Dynamical screening and excitonic instability in bilayer graphene. *Phys. Rev. Lett.* **104**, 156803 (2010).
23. Fradkin, E., Kivelson, S. A., Lawler, M. J., Eisenstein, J. P. & Mackenzie, A. P. Nematic Fermi fluids in condensed matter physics. *Annu. Rev. Condens. Matter Phys.* **1**, 153–178 (2010).
24. Fu, L. Parity-breaking phases of spin–orbit-coupled metals with gyrotropic, ferroelectric, and multipolar orders. *Phys. Rev. Lett.* **115**, 026401 (2015).
25. Fernandes, R. M. & Venderbos, J. W. Nematicity with a twist: rotational symmetry breaking in a moiré superlattice. *Sci. Adv.* **6**, eaba8834 (2020).
26. Kozii, V. & Fu, L. Odd-parity superconductivity in the vicinity of inversion symmetry breaking in spin–orbit-coupled systems. *Phys. Rev. Lett.* **115**, 207002 (2015).
27. Mishra, A. & Lee, S. Topological multiferroic phases in the extended Kane–Mele–Hubbard model in the Hofstadter regime. *Phys. Rev. B* **98**, 235124 (2018).
28. Cao, Y. et al. Nematicity and competing orders in superconducting magic-angle graphene. Preprint at https://arxiv.org/abs/2004.04148 (2020).
29. Jiang, Y. et al. Charge order and broken rotational symmetry in magic-angle twisted bilayer graphene. *Nature* **573**, 91–95 (2019).
30. Choi, Y. et al. Imaging electronic correlations in twisted bilayer graphene near the magic angle. *Nat. Phys.* **15**, 1174–1180 (2019); correction **15**, 1205 (2019).
31. Zhang, Y.-H., Mao, D., Cao, Y., Jarillo-Herrero, P. & Senthil, T. Nearly flat Chern bands in moiré superlattices. *Phys. Rev. B* **99**, 075127 (2019).
32. McCann, E. & Koshino, M. The electronic properties of bilayer graphene. *Rep. Prog. Phys.* **76**, 056503 (2013).
33. Li, J., Martin, I., Büttiker, M. & Morpurgo, A. F. Topological origin of subgap conductance in insulating bilayer graphene. *Nat. Phys.* **7**, 38–42 (2011).
34. Ju, L. et al. Topological valley transport at bilayer graphene domain walls. *Nature* **520**, 650–655 (2015).
35. Sui, M. et al. Gate-tunable topological valley transport in bilayer graphene. *Nat. Phys.* **11**, 1027–1031 (2015).
36. Shimazaki, Y. et al. Generation and detection of pure valley current by electrically induced Berry curvature in bilayer graphene. *Nat. Phys.* **11**, 1032–1036 (2015).
37. Ju, L. et al. Tunable excitons in bilayer graphene. *Science* **358**, 907–910 (2017).
38. Maher, P. et al. Evidence for a spin phase transition at charge neutrality in bilayer graphene. *Nat. Phys.* **9**, 154–158 (2013).
39. Hunt, B. et al. Direct measurement of discrete valley and orbital quantum numbers in bilayer graphene. *Nat. Commun.* **8**, 948 (2017).
40. Weitz, R. T., Allen, M., Feldman, B., Martin, J. & Yacoby, A. Broken-symmetry states in doubly gated suspended bilayer graphene. *Science* **330**, 812–816 (2010).
41. Bao, W. et al. Evidence for a spontaneous gapped state in ultraclean bilayer graphene. *Proc. Natl Acad. Sci. USA* **109**, 10802–10805 (2012).
42. Freitag, F., Trbovic, J., Weiss, M. & Schönenberger, C. Spontaneously gapped ground state in suspended bilayer graphene. *Phys. Rev. Lett.* **108**, 076602 (2012).
43. Nam, Y., Ki, D.-K., Soler-Delgado, D. & Morpurgo, A. F. A family of finite-temperature electronic phase transitions in graphene multilayers. *Science* **362**, 324–328 (2018).
44. Fei, Z. et al. Ferroelectric switching of a two-dimensional metal. *Nature* **560**, 336–339 (2018).
45. Zhang, Y., Yuan, N. F. & Fu, L. Moiré quantum chemistry: charge transfer in transition metal dichalcogenide superlattices. Preprint at https://arxiv.org/abs/1910.14061 (2019).
46. Katayama, Y., Tsui, D., Manoharan, H., Parihar, S. & Shayegan, M. Charge transfer at double-layer to single-layer transition in double-quantum-well systems. *Phys. Rev. B* **52**, 14817–14824 (1995).

Methods

Device fabrication and rotational alignment

We fabricated BN-encapsulated Bernal-stacked BLG devices with different alignment configurations between graphene and BN. Graphene and BN flakes were first exfoliated onto silicon/silicon dioxide chips. BLG was identified using Raman spectroscopy. BN flakes with suitable thicknesses (between 10 nm and 50 nm) were chosen based on optical contrast and later measured by atomic force microscopy. In addition, we chose graphene and BN flakes with long and straight edges, which, with high likelihood, correspond to one of the crystallographic axes (armchair or zigzag). Therefore, the straight edges can be used as a guide for rotational alignment between different flakes. The bottom BN, graphene and the top BN flakes were stacked together and transferred onto pre-patterned metal bottom gates through the standard dry transfer technique using a polydimethylsiloxane/poly(bisphenol A carbonate) stamp. In devices H1, H2 and H3, the top and bottom BN were from two independent flakes. We intentionally aligned the straight edges of only the top BN (for H1 and H3) or both the top and bottom BN (for H2) to that of graphene. In device H4, we used the reactive ion etching method to cut one large BN flake into two pieces and used them for both the top and bottom BN layers. The straight edges of the top and bottom BN (originally the same edge in this case) and graphene were all aligned for device H4. Electrical connections to the devices were made through a top contact method: we first used electron beam lithography to define electrode areas, then etched the top BN within those areas and evaporated chromium/palladium/gold on top of the now exposed graphene. In some of our devices, a protective layer of BN was transferred on top of the device before the top gate (metal or monolayer graphene) was fabricated (details specified in Extended Data Table 1). In the dual-gate (top gate voltage V_{TG} and bottom gate voltage V_{BG}) structure, the externally injected carrier density, n_{ext}, is defined as $n_{ext} = \frac{\varepsilon_b \varepsilon_0 V_{BG}}{e d_b} + \frac{\varepsilon_t \varepsilon_0 V_{TG}}{e d_t}$ and the externally defined displacement field as $D_{ext} = \frac{1}{2}\left(\frac{\varepsilon_b \varepsilon_0 V_{BG}}{d_b} - \frac{\varepsilon_t \varepsilon_0 V_{TG}}{d_t}\right)$. D_{ext}/ε_0 is the effective electric field applied to the BLG through the combination of the top and bottom gates, following many of the previous studies[39,44,47,48]. Here, ε_0 is the vacuum permittivity, $\varepsilon_{b(t)}$ is the bottom (top) gate dielectric constant and $d_{b(t)}$ is the thickness of bottom (top) BN flake. In devices H2 and H4, however, the prominent hysteretic behaviour imposes challenges on the conversion based on the definition above. Therefore, we define n_{ext} and D_{ext} based on the Hall density measurement and the resistance peak slope in the dual-gate map in the 'normal BLG' region. For the same device, we keep a constant conversion for all the data presented.

We performed optical second-harmonic generation measurements to determine the crystallographic axes of BN[49] and therefore the relative rotational angles between the top and bottom BN flakes for devices H1, H2 and H3. The measurements (Supplementary Section V.1) show that for devices H1 and H3, the top and bottom BN was rotated by about 20° (or 80°). For device H2, the top and bottom BN was rotated by about 30° (or 90°). This is not surprising, as the straight edge can be along either the zigzag or armchair direction in honeycomb lattices. In device H4, the top and bottom BN originates from the same flake. However, the relative alignment angle between the top and bottom BN can still be 0° or 180°. This is because of the natural stacking sequence of the BN crystal: each BN layer is 180° rotated with respect to its neighbour. Therefore, depending on the evenness or oddness of the number of layers of the BN flake, the two BN layers that directly interface with the BLG can have a relative angle of 0° or 180°. This angle certainly can affect the top and bottom moiré patterns, which in turn affect the moiré bandstructure. However, they cannot be distinguished by our current fabrication and deserve future investigation.

For devices H1 and H3, we can extract the moiré wavelength and twist angle between graphene and BN from the carrier density at the superlattice gaps, which correspond to the full filling of the moiré bands (four electrons per moiré unit cell). The moiré wavelength λ and the twist angle ϕ are related to the superlattice density n_s as follows[50]:

$$\lambda = \frac{(1+\delta)a}{\sqrt{2(1+\delta)(1-\cos\phi)+\delta^2}}, \quad \frac{g_s g_v 2}{\sqrt{3}\lambda^2} = n_s$$

where a is graphene lattice constant, δ is the lattice mismatch between BN and graphene, and g_s and g_v are the spin and valley degeneracies. Owing to the lattice mismatch, it has been previously shown that the graphene/BN superlattice with both zero or small twist angles can give rise to a moiré pattern with long wavelength[50–54]. For both device H1 and device H3, the moiré wavelength is about 10 nm, corresponding to a twist angle of about 1°. For devices H2 and H4, it is difficult to identify superlattice peaks due to the prominent hysteretic behaviour of carrier density with gating (see Supplementary Section V for more information).

Summary of device parameters and basic behaviour

We have measured a spectrum of different dual-gated graphene devices, including monolayer graphene (MLG), Bernal-stacked BLG and ABA trilayer graphene (TLG) with various alignment configurations to the top and bottom BN. Among these devices, we only observed substantial hysteretic behaviour with the displacement field in aligned BLG devices. In these devices, the BLG and the top and/or bottom BN are stacked with special angles. The parameters of the hysteretic devices and representative control devices are summarized in Extended Data Table 1 and further explained in the text below. Here we use M for monolayer, N for normal bilayer, T for trilayer and H for hysteretic devices.

To further illustrate the behaviour of different devices and compare their responses to the out-of-plane displacement field, we highlight some of the key devices in Extended Data Fig. 1.

Device M1. In Extended Data Fig. 1a–c, we show the behaviour of a double-aligned MLG device. The resistance map is characterized by insulating regimes (high resistance) along the top-left to bottom-right diagonal line with multiple series of superlattice peaks corresponding to different moiré wavelengths due to the close alignment of all three components. No hysteresis is observed as we sweep the displacement field back and forth.

Device N0. In Extended Data Fig. 1d–f, for the unaligned BLG device N0, we indeed observe the normal BLG transport behaviour, as observed in many previous studies[47,55]. The resistance map is characterized by insulating regimes (high resistance) along the top-left to bottom-right diagonal line with a displacement-field-dependent gap-opening behaviour but metallic regimes (low resistance) elsewhere. No hysteresis is observed as we sweep the displacement field back and forth.

Device T1. In Extended Data Fig. 1g–i, we show the behaviour of an aligned TLG device. Instead of a gap-opening behaviour along the displacement field, we note that the high-resistance area is near the zero-displacement-field region and decreases as the displacement field increases. This is consistent with what is reported for the case of ABA stacked TLG[56,57]. As with the normal BLG, we do not see an obvious sign of hysteresis when we scan along the displacement-field direction.

Device H1/H3. Devices H1 and H3 have the same stacking configurations between the BLG and BN layers and show the same hysteretic characteristics. We show measurements from device H1 in Extended Data Fig. 1k–m. The resistance of the Dirac peak is asymmetric about the zero-displacement field. Depending on the scanning direction, the resistance in the positive-displacement-field side is higher (or lower) than that in the negative-displacement-field side. This hysteretic behaviour is better visualized in Extended Data Fig. 1m, where the forward and backward curves form a closed hysteresis loop.

Device H2/H4. We classify devices H2 and H4 in the same group with strong hysteresis. 'Strong' is defined as follows. (1) There is striking switching between the 'normal dual gating' and 'layer-specific anomalous screening' (LSAS) regimes. In the LSAS regime, the resistance peak runs parallel to a single gate in the dual-gate map (Extended Data Fig. 1o). (2) In the n–D map (Extended Data Fig. 1p), between the forward and backward displacement field scans, the resistance peak lines have a substantial shift in terms of the externally defined carrier density. (3) In both the dual-gate V_{BG}–V_{TG} map and n–D map, there is dramatic asymmetry both between $+D$ and $-D$ and between electron and hole. Points (1), (2) and (3) are closely linked. The strong hysteretic behaviour is the focus of our analyses in the paper.

Distinguishing the intrinsic and extrinsic mechanism

Below, we discuss the possibility that our observations, including the strong hysteresis and the LSAS phenomena, are caused by trapped extrinsic charges. Of particular importance is to address the possibility of extrinsic charge injection into the BLG system by the applied gate voltages. We consider two possible extrinsic trapping sites: defects in the BN dielectrics and at the graphene/BN moiré interfaces. They are both unlikely due to the following experimental facts. (1) Let us assume that the hysteresis arises from extrinsic charges in a particular BN layer (for example, the bottom BN). Given the fact that the BLG is electrically grounded, the top gate voltage V_{TG} will not be able to apply any substantial electric field in the bottom BN dielectric. In other words, the switching, in this case, will only depend strongly on V_{BG} and will be nearly independent of V_{TG}. In contrast, in our data, the switching depends on D_{ext}, which is accomplished by scanning V_{TG} and V_{BG} in a coordinated manner. This clearly shows that the ferroelectric switching arises from the BLG itself, rather than from defects (charge injections) from the dielectric layer on a single side. (2) We have studied carefully aligned MLG/BN moiré systems and ABA TLG/BN moiré systems. The results are consistent with previous studies[13,51–54]. They do not show the hysteresis as observed in devices H2 and H4. (3) We have studied many BLG/BN devices (including devices H1–H4 and additional devices shown in Methods). We fabricated these devices using the same procedures but with various relative alignment angles between the three components (bottom BN, graphene and top BN). The hysteresis is found to be uniquely tied to the relative alignment angles. (4) In Supplementary Section V.2, we present additional data from device H2, which shows that the hysteresis behaviour is indeed sensitive to very small angle variations across the sample. (5) In previous studies, hysteresis caused by extrinsic charge trapping states is found to strongly depend on the gate sweeping rate[58]. In contrast, our measurements (Extended Data Fig. 8) show that the observed hysteresis is independent of gate sweeping rates. In Supplementary Section II, we expand on the above discussion and also provide additional pieces of evidence. These systematic measurements and analyses, taken collectively, strongly suggest that extrinsic charge traps are highly unlikely, indicating an intrinsic origin of the observed ferroelectricity.

Our systematic measurements provide important clues towards understanding the microscopic mechanism for the observed ferroelectricity. In conventional ferroelectrics, the ions spontaneously displace in an ordered fashion that breaks crystalline inversion symmetry, leading to an electrical polarization. Such a lattice model is less likely here based on the combination of our theoretical analyses and experimental observations. (1) In a pristine BN-aligned BLG lattice, no macroscopic electrical polarization is expected. This is because, while boron and nitrogen provide opposite local potentials to carbon, the existence of the moiré pattern leads to cancellation upon spatial average (see analyses in Supplementary Section II.2). (2) The sharpness of features in the resistance and capacitance maps (Extended Data Fig. 7), as well as the consistency over many consecutive scans, indicate that the ferroelectric switching is uniform over the entire sample, rather than from local structures on the moiré scale[59]. (3) More importantly, the LSAS behaviour is beyond what is expected for conventional ferroelectric materials. In a conventional ferroelectric material, positive and negative bound charges move under the influence of the external displacement field, flipping the polarization. Notably, the displacement field only flips the polarization but does not change the number of total mobile carriers. This is the case for all well-studied ferroelectric materials (being insulators with zero carrier density before and after the switching). This is also the case for the recently discovered ferroelectric metal, few-layer tungsten telluride (WTe_2). Despite the presence of free carriers, in WTe_2, the total mobile carrier density remains unchanged before and after the switching via the displacement field[44]. In sharp contrast, here we observe that, because of the LSAS behaviour, the displacement field can change the total mobile carrier density of the BLG, as demonstrated by the Hall measurements.

Understandings on the relation between device H2 and device H4

While the microscopic picture in the main text was described based on device H4, behaviours in both devices can be understood consistently within the same picture. One noticeable difference in detailed behaviour between device H2 and device H4 is the opposite sequence between normal BLG and the LSAS regime as we described in the main text. We may understand this difference by assuming that in device H4, a minimum D_{ext} is needed to generate the flat band, whereas, in device H2, a layer-specific moiré flat band may be already present close to the Fermi level at $D_{ext} = 0$. Such an assumption requires that the flatness of the band depends both on the displacement field and the details of the moiré potential, which is quite likely in Bernal BLG. Indeed, recent experiments on twisted double BLG show correlated insulator behaviour for only intermediate displacement-field ranges[15–18]. In our system, the moiré bandstructure will depend on delicate geometrical properties. One obvious geometrical property is the stacking angle. Another geometrical property relevant in device H4 is the translational alignment between the two moiré patterns. As the graphene layers in device H4 are rotationally aligned with both BN flakes, the moiré patterns from both sides are expected to be very similar in terms of moiré unit cell structure and wavelength. Thus, the translational alignment between the two moiré patterns in device H4 may be important. In summary, the coexistence and independent configuration of the top-BN/graphene moiré potential and bottom-BN/graphene moiré potential, together with applying a displacement field can fine-tune both the single-particle bandstructures and the correlation landscape, giving rise to different behaviours in devices H4 and H2.

Probing the out-of-plane electrical polarization using the MLG sensor

In device H4, which has MLG as its top gate, we can also probe the out-of-plane polarization by using the top monolayer graphene (tp-MLG) as an electric-field sensor, a technique demonstrated in ref. [44]. The MLG conductance serves as a direct measurement of the electrical field inside the top BN dielectric (E_t). To then relate E_t to the electrical polarization P (areal polarization density, with unit $\mu C\,cm^{-2}$) of the BLG, we define E_i as the interlayer electric field and d_i as the interlayer distance of the BLG. We have the relation $\varepsilon_0\varepsilon_t E_t = \varepsilon_0 E_i + P$ directly following Gauss's law. Further, for the case that the MLG and BLG are both grounded and the BLG is at charge neutrality, we have another relation $E_t d_t + E_i(\frac{1}{2}d_i) = 0$. According to the two relations above, P directly depends on E_t through $P = (\varepsilon_0\varepsilon_t d_i + 2\varepsilon_0 d_t)(E_t/d_i)$. As $d_t \gg d_i$, $P \approx 2\varepsilon_0(d_t/d_i)E_t$. Now, we consider two states of the bilayer with opposite electrical polarizations but with zero net charge. The change of polarization ΔP between these two states is directly proportional to the corresponding changes of the top electric field ΔE_t: $\Delta P \approx 2\varepsilon_0(d_t/d_i)\Delta E_t$.

As a reference, we first measure the tp-MLG conductance as a function of the gate voltage applied between the BLG and the tp-MLG, V_{BL} (Extended Data Fig. 6e, f). This allows us to uniquely assign a

corresponding value of E_t to each value of the tp-MLG conductance through the relation $E_t = V_{BL}/d_t$ (V_{BL} can be read from the x axis) (assuming we know whether the monolayer is electron doped or hole doped). Now, we ground both the tp-MLG and the BLG, and measure the MLG conductance as we vary the bottom gate voltage V_{BG}. As shown in Extended Data Fig. 6d, the tp-MLG conductance shows a substantial hysteresis when we scan V_{BG} forward and backward. In particular, the tp-MLG shows two different conductance values when the BLG has opposite polarization but remains charge neutral (as a comparison between Extended Data Fig. 6d and Extended Data Fig. 6b shows). By extracting V_{BL} values corresponding to these two tp-MLG conductance values, we obtain $\Delta P \approx 2\varepsilon_0 \Delta V_{BL}/d_i \approx 0.12\ \mu C\ cm^{-2}$.

This value is on the same order of magnitude as the one obtained from Fig. 3, but the specific value differs by a factor of 2.4. We provide one possible reason for this discrepancy. For simplicity, we refer to the method used in Fig. 3 as method I and the method used in Extended Data Fig. 6 as method II. In method I, ΔP is extracted according to $\varepsilon_0 E_i + P = 0$ (effective displacement field is zero between the top and bottom layers of the BLG) at the gapless point of the BLG. In method II, ΔP is extracted according to $E_t d_t + E_i\left(\frac{1}{2}d_i\right) = 0$, meaning the potential drop between the centre of the BLG and the tp-MLG is zero when they are both grounded. Experimentally, the potential at the centre of the BLG may not be strictly zero.

Probing the electronic compressibility through capacitance measurements

To further confirm the dramatic hysteretic behaviour observed in transport measurements, we also performed capacitance measurements, which are sensitive to the bulk properties of the entire device area rather than local electronic behaviour. Owing to the low dimensionality of BLG, the capacitance measured between the graphene and one of the gates contains a notable contribution from the electronic compressibility, a thermodynamic measure of the density of states. In a 2D system with a single gate, the capacitance is related to the compressibility through a quantum capacitance term, $C_q \equiv Ae^2\partial n/\partial\mu$ (A is the area of the capacitor and μ is the chemical potential), which sums in series with the geometric capacitance C_g to yield the total capacitance, $C^{-1} = C_g^{-1} + C_q^{-1}$. In BLG with top and bottom gates, there is a similar relation for each of the top and bottom capacitances, with additional terms due to the coupling between the layers.

Here we focus on bottom-gate capacitance data from device H2, measured in a 4-K helium cryostat with an excitation voltage of $\delta V_{BG} = 1$ mV at 57.3 kHz. The off-balance signal from a capacitance bridge (point (B) in Extended Data Fig. 7e) is amplified using a cryogenic two-stage amplifier to remove the effect of stray capacitances from measurement cabling. The capacitance was calculated by relating the off-balance voltage to a reference capacitance on the bridge circuit.

By measuring the bottom-gate capacitance C_b while sweeping the gate-defined displacement field, D_{ext}, for a series of fixed gate-defined carrier densities, n_{ext}, we directly map the parameters for which the bulk of the bilayer becomes incompressible (dark lines in Extended Data Fig. 7a), denoting the opening of a bandgap. Normally, in intrinsic BLG, there is a bandgap at charge neutrality that depends monotonically on the magnitude of the displacement field. However, in our experiment, the incompressible feature deviates from $n_{ext} = 0$ for a large range of displacement fields. Sweeping the external field in the opposite direction (Extended Data Fig. 7b) results in a large shift in the position of this feature, in good agreement with the shift of the resistive state, observed in transport (Extended Data Fig. 5a, b). The hysteretic path of this incompressible state, and the correspondence between capacitance dips and resistance peaks, as shown in Extended Data Fig. 7c, d, crucially confirms that the resistance switching behaviour observed in transport is a bulk property of the BLG.

Data availability

The data that support the plots within this paper and other findings of this study are available from the corresponding authors upon reasonable request.

47. Zhang, Y. et al. Direct observation of a widely tunable bandgap in bilayer graphene. *Nature* **459**, 820–823 (2009).
48. Young, A. F. & Levitov, L. S. Capacitance of graphene bilayer as a probe of layer-specific properties. *Phys. Rev. B* **84**, 085441 (2011).
49. Li, Y. et al. Probing symmetry properties of few-layer MoS_2 and h-BN by optical second-harmonic generation. *Nano Lett.* **13**, 3329–3333 (2013).
50. Yankowitz, M. et al. Emergence of superlattice Dirac points in graphene on hexagonal boron nitride. *Nat. Phys.* **8**, 382–386 (2012).
51. Dean, C. R. et al. Hofstadter's butterfly and the fractal quantum Hall effect in moiré superlattices. *Nature* **497**, 598–602 (2013).
52. Ponomarenko, L. et al. Cloning of Dirac fermions in graphene superlattices. *Nature* **497**, 594–597 (2013).
53. Hunt, B. et al. Massive Dirac fermions and Hofstadter butterfly in a van der Waals heterostructure. *Science* **340**, 1427–1430 (2013).
54. Finney, N. R. et al. Tunable crystal symmetry in graphene–boron nitride heterostructures with coexisting moiré superlattices. *Nat. Nanotechnol.* **14**, 1029–1034 (2019).
55. Novoselov, K. S. et al. Unconventional quantum Hall effect and Berry's phase of 2π in bilayer graphene. *Nat. Phys.* **2**, 177–180 (2006).
56. Craciun, M. et al. Trilayer graphene is a semimetal with a gate-tunable band overlap. *Nat. Nanotechnol.* **4**, 383–388 (2009).
57. Jhang, S. H. et al. Stacking-order dependent transport properties of trilayer graphene. *Phys. Rev. B* **84**, 161408 (2011).
58. Wang, H., Wu, Y., Cong, C., Shang, J. & Yu, T. Hysteresis of electronic transport in graphene transistors. *ACS Nano* **4**, 7221–7228 (2010).
59. McGilly, L. et al. Visualization of moiré superlattices. *Nat. Nanotechnol.* **15**, 580–584 (2020).

Acknowledgements We thank D. Bandurin, V. Fatemi, L. Levitov, Y. Lin, J. Mundy, R. Ramesh, J. Sanchez-Yamagishi, H. Shen, J. Song, S. Todadri, A. Vishwanath and N. Yuan for discussions; and T. Dinh for initial efforts on this project. Work in the P.J.-H. group was supported by the US DOE, BES Office, Division of Materials Sciences and Engineering under award DE-SC0001819 (device fabrication and transport measurements), the Center for the Advancement of Topological Semimetals, an Energy Frontier Research Center funded by the US Department of Energy Office of Science, through the Ames Laboratory under contract DE-AC02-07CH11358 (data analysis), and the Gordon and Betty Moore Foundation's EPiQS Initiative through grant GBMF9643 to P.J.-H. The development of new nanofabrication and characterization techniques enabling this work has been supported by the US DOE Office of Science, BES, under award DE-SC0019300. Partial support for measurement and characterization training was through AFOSR grant FA9550-16-1-0382. This work made use of the Materials Research Science and Engineering Center Shared Experimental Facilities supported by the National Science Foundation (NSF) (grant number DMR-0819762). N.G. and S.-Y.X. acknowledge support from DOE, BES DMSE (data taking and analysis), and National Science Foundation under grant number DMR-1809815 (manuscript writing). K.W. and T.T. acknowledge support from the Elemental Strategy Initiative conducted by the MEXT, Japan, grant number JPMXP0112101001, JSPS KAKENHI grant numbers JP20H00354 and the CREST(JPMJCR15F3), JST. R.A. (capacitance measurements), Z.B., Y.Z. and L.F. (theory) acknowledge support from NSF Science and Technology Center for Integrated Quantum Materials grant DMR-1231319. M.-H.L. was supported by Taiwan Ministry of Science and Technology (MOST) under grant numbers 109-2112-M-006-020-MY3 and 108-2638-M-006-002-MY2. N.M. and J.K. acknowledge the support by the US Department of Energy (DOE), Office of Science, Basic Energy Sciences (BES) under award DE-SC0020042.

Author contributions Q.M. and S.-Y.X. conceived the idea and experiment. Z.Z. fabricated devices, performed transport measurements and analysed data under the supervision of Q.M. and P.J.-H. S.d.l.B. performed capacitance measurements with the help of Z.Z. under the supervision of R.A. Z.B., Y.Z. and N.K. performed theoretical modelling and bandstructure calculations under the supervision of S.-Y.X., Q.M., N.G. and L.F. M.-H.L. performed the simulation of the transport behaviours for the hysteretic devices. N.M. performed second-harmonic generation measurements of BN flakes under the supervision of J.K. and W.A.T. K.W. and T.T. grew the bulk BN single crystals. All authors discussed the results and wrote the manuscript.

Competing interests The authors declare no competing interests.

Additional information

Supplementary information is available for this paper at https://doi.org/10.1038/s41586-020-2970-9.

Correspondence and requests for materials should be addressed to Q.M. or P.J.-H.

Peer review information *Nature* thanks Kayoung Lee and the other, anonymous, reviewer(s) for their contribution to the peer review of this work.

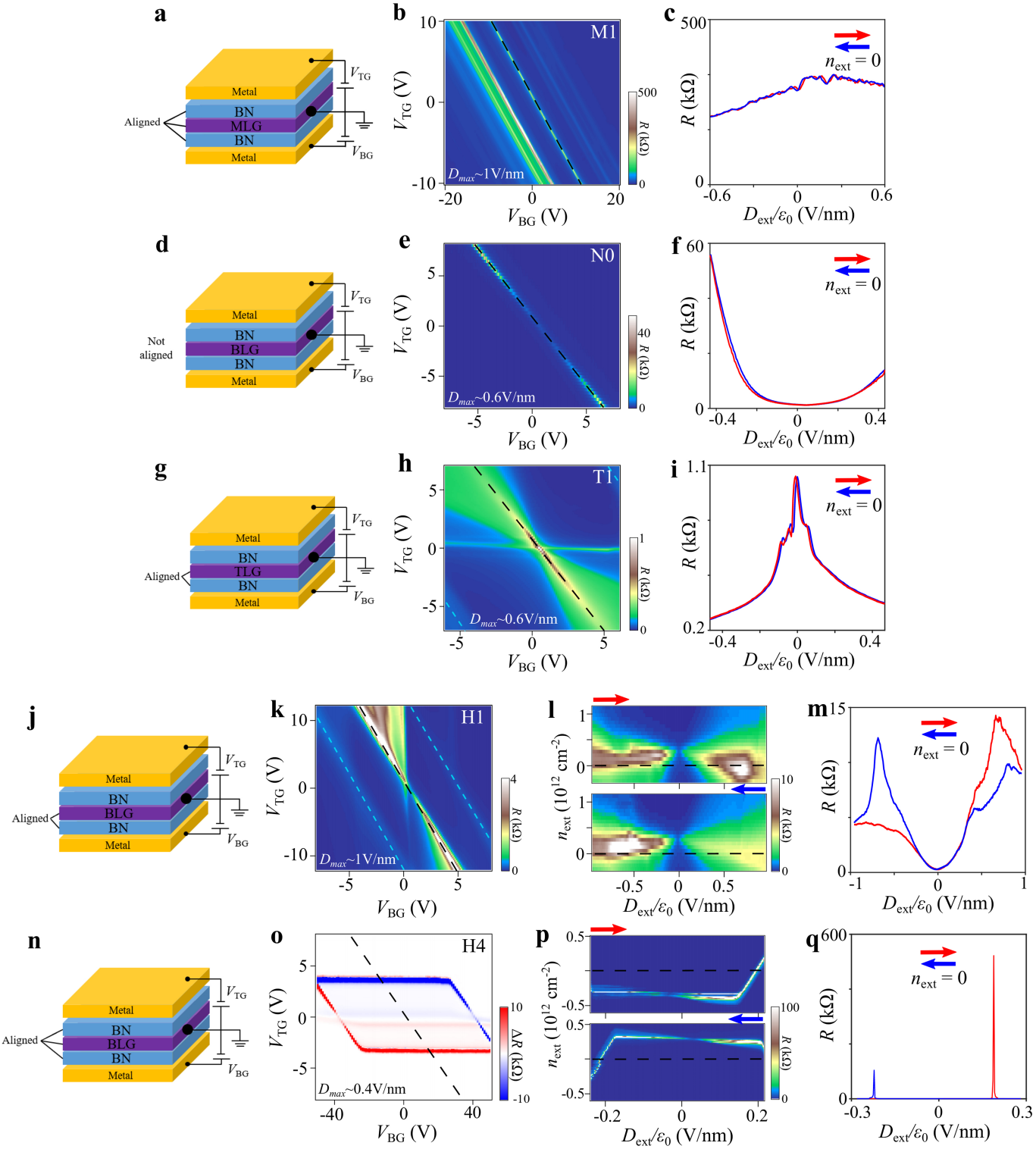

Extended Data Fig. 1 | Resistance data summary for devices M1, N0, T1, H1 and H4. Device schematic (**a**, **d**, **g**, **j**, **n**), dual-gate resistance map (**b**, **e**, **h**, **k**, **o**), *n*–*D* map (forward and backward) (**l**, **p**), and resistance as a function of externally applied displacement field at zero doping (**c**, **f**, **i**, **m**, **q**) for representative devices M1 (**a**–**c**), N0 (**d**–**f**), T1 (**g**–**i**), H1 (**j**–**m**) and H4 (**n**–**q**). The line traces along the electric-field direction are marked by black dashed lines. The superlattice resistance peaks are marked by cyan dashed lines. Note that the horizontal resistance line in **h** stems from a region of the sample that is only controlled by the top gate. Note that line traces in **q** are taken at $n_{ext} = 0$ from the *n*–*D* map (**p**), whereas line traces in Fig. 1f in the main text are taken at $V_{TG} = 0$ from the dual-gate map (Supplementary Fig. 25e, f), hence the difference in resistance magnitude.

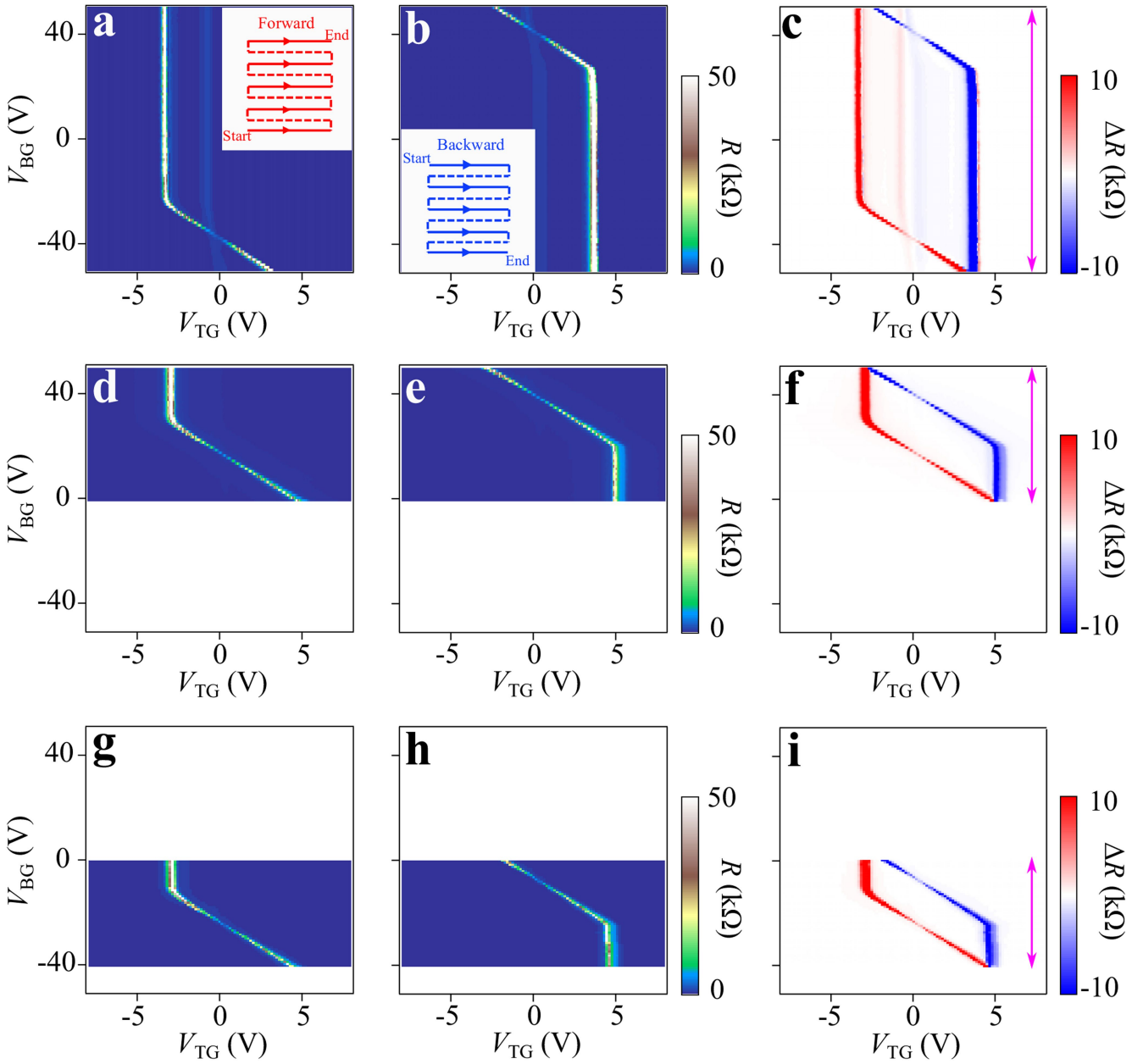

Extended Data Fig. 2 | Shifting of the hysteretic behaviour in device H4. **a**–**c**, Forward (**a**) and backward (**b**) scans of the four-probe longitudinal resistance as a function of V_{TG} and V_{BG} and their difference (**c**). **d**–**f**, **g**–**i**, Same measurements as in **a**–**c**, except that V_{BG} is swept between 0 V and 50 V (**d**–**f**) and between −40 V and 0 V (**g**–**i**). We present a phenomenological model to simulate the resistance maps in Supplementary Section V.3.2.

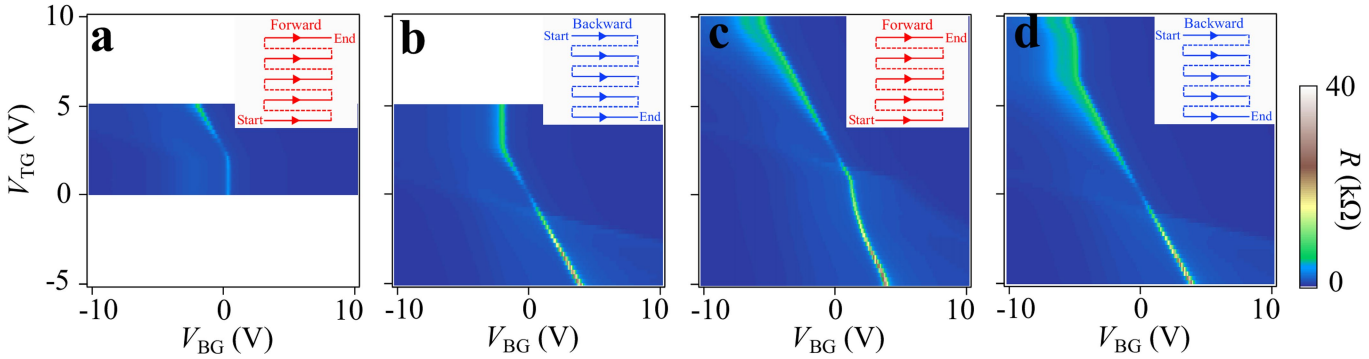

Extended Data Fig. 3 | Hysteretic transport behaviour for device H2. a–**d**, The four-probe resistance as a function of V_{BG} (range, −10 V to 10 V) and V_{TG} with ranges from 0 V to 5 V (**a**), from 5 V to −5 V (**b**), from −5 V to 10 V (**c**), and from 10 V to −5 V (**d**). The scan sequences are specified in the insets.

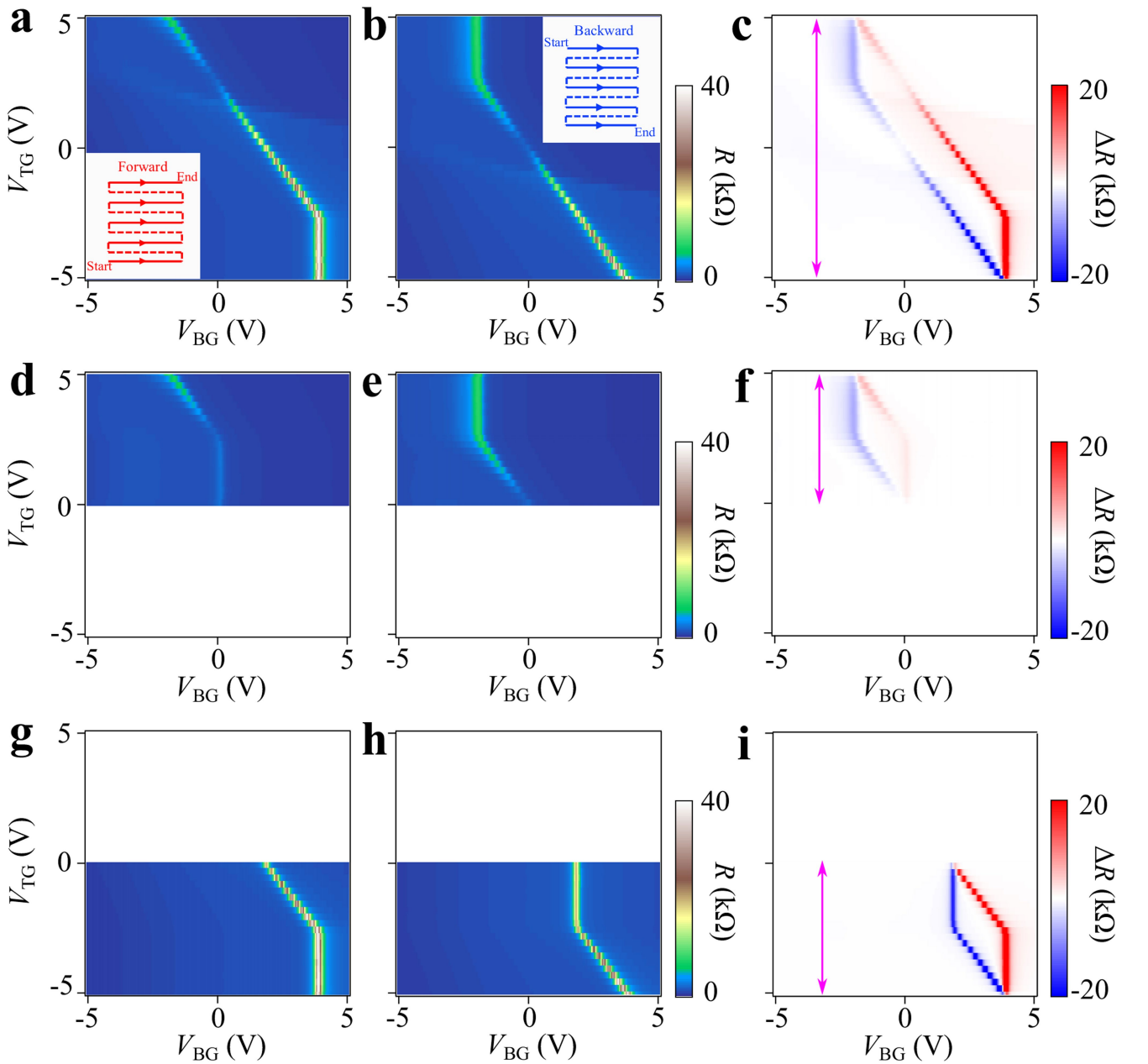

Extended Data Fig. 4 | Shifting of the hysteretic behaviour in device H2. **a**–**c**, Four-probe longitudinal resistance as a function of V_{TG} and V_{BG} for the forward (**a**) and backward (**b**) scans and their difference (**c**). **d**–**i**, Same measurements as in **a**–**c**, except that V_{TG} is measured within 0 V to 5 V (**d**–**f**) and within −5 V to 0 V (**g**–**i**).

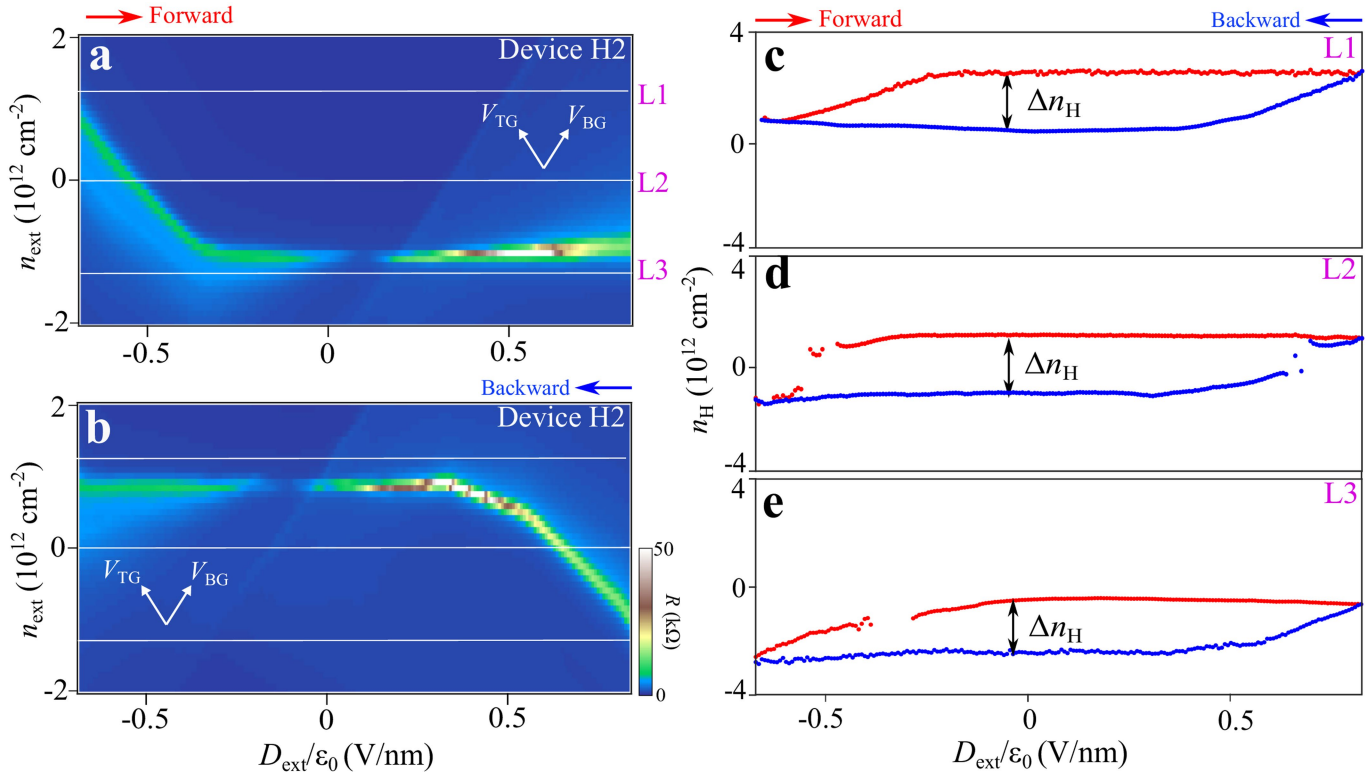

Extended Data Fig. 5 | Hysteretic signature in Hall measurements for device H2. a, **b**, The resistance measured while sweeping the externally applied displacement field D_{ext} in the forward (**a**) and backward (**b**) direction at each fixed carrier density n_{ext}. The carrier density scan direction is from the negative to positive values. **c**–**e**, Carrier density extracted from Hall measurements along the lines L1 (**c**), L2 (**d**) and L3 (**e**) denoted in **a**. Red and blue curves were taken during the forward and backward scan of D_{ext}, respectively.

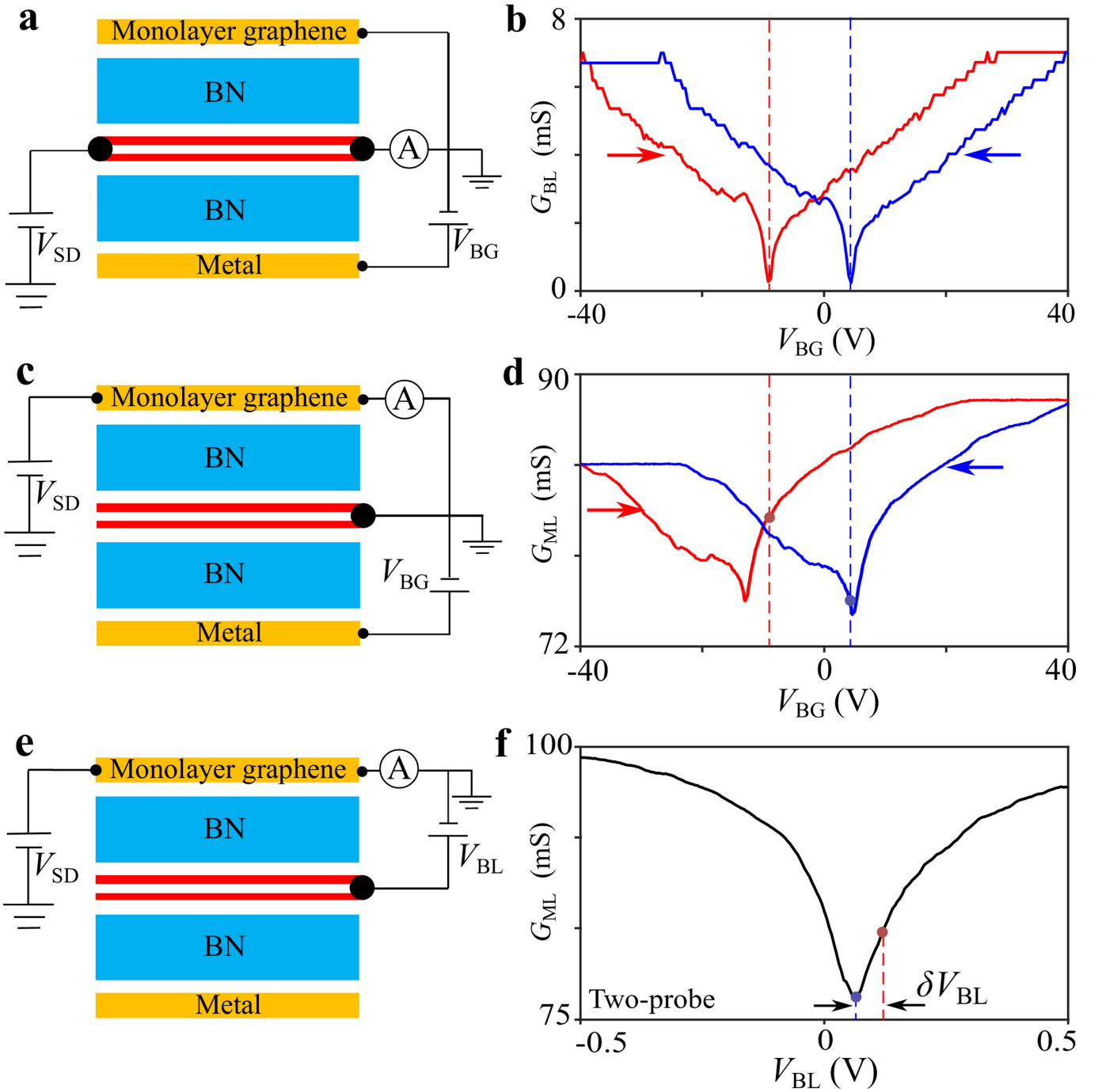

Extended Data Fig. 6 | Probing the out-of-plane electrical polarization using the top MLG sensor in device H4. a, Experimental configuration for measurements of the conductance of the BLG. **b**, Measured conductance of the BLG as a function of V_{BG} (top gate is grounded). The red and blue curves correspond to the forward and backward V_{BG} scans, respectively. The vertical dashed lines denote the V_{BG} values that correspond to the charge-neutrality point of the BLG for forward and backward scans. **c**, Experimental configuration for the measurements of the conductance of the tp-MLG with gate voltage V_{BG} applied to bottom metal gate and the BLG grounded. **d**, Measured conductance of the tp-MLG as a function of V_{BG} with the experimental configuration in **c**. The gate voltages are the same as in **b** (Methods). The red and blue dots denote the conductance of the tp-MLG when the BLG is charge neutral. **e**, Experimental configuration for the measurements of the conductance of the tp-MLG with gate voltage V_{BL} applied to the BLG. **f**, Measurements of the conductance of the tp-MLG as a function of V_{BL} with the experimental configuration in **e**. The conductance of the monolayer at the red and blue dots in **d** can be inversely mapped to two different V_{BL} values, which corresponds to the difference of electrostatic potentials on the top surface of BLG induced by ferroelectric switching (Methods). The in-plane bias voltage V_{SD} was kept below 1 mV for all the measurements.

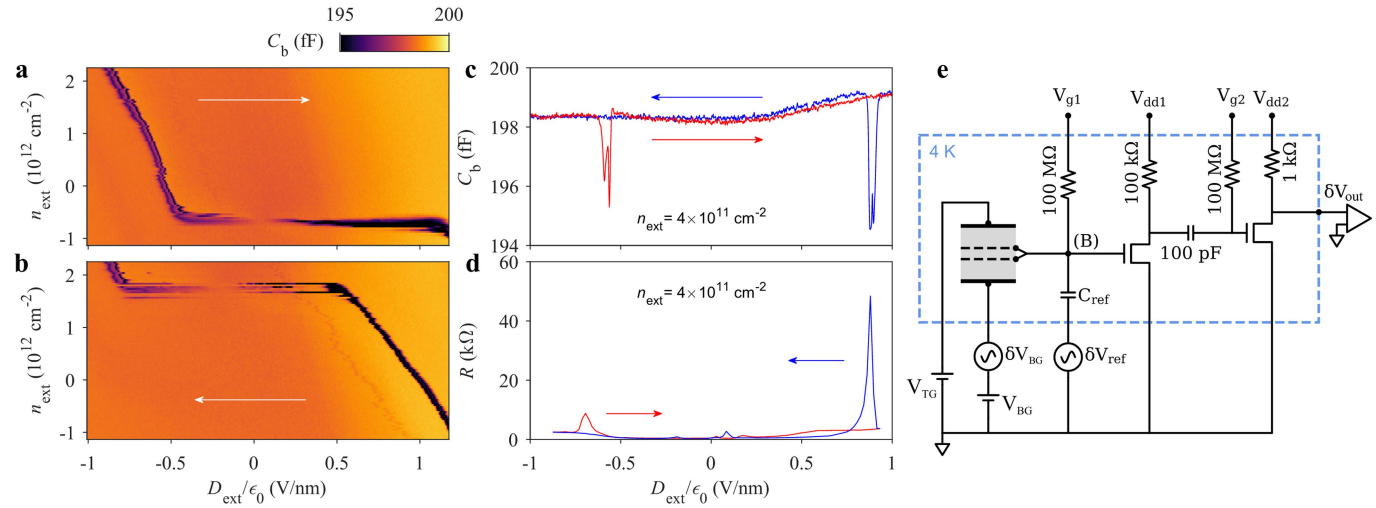

Extended Data Fig. 7 | Hysteresis signature in the bulk electronic compressibility of device H2. a, **b**, Bottom capacitance C_b between the bottom gate and BLG as a function of the externally applied field, D_{ext} as the fast-scan axis, and gate-defined carrier density, n_{ext} as the slow-scan axis. The white arrows indicate the sweep direction of D_{ext} in each panel. Deviations of the capacitance from the geometric value reflect modulations in the electronic compressibility, $\partial n/\partial \mu$, from the total area of BLG overlapping the bottom gate. Data were collected by sweeping the displacement field at each fixed carrier density, as in Fig. 2h, i. Dark features indicate regions of incompressibility resulting from the opening of a gap in the BLG. The gapless point, a compressible state with high C_b, is achieved at a finite D_{ext} that depends on the sweep direction. **c**, Forward and backward traces from **a** and **b** at a fixed n_{ext}. **d**, Resistance traces at the same density showing resistance peaks corresponding to the incompressible features in **c**. **e**, Circuit schematic of the bottom gate capacitance measurement, including a two-stage cryogenic amplifier (enclosed in dashed box). Capacitance is measured by applying a small a.c. excitation voltage to the bottom gate, δV_{BG}, while also applying a nearly 180° out-of-phase signal, δV_{ref}, to a reference capacitor, C_{ref} to null the voltage at the bridge balance point, (B). Deviations in the balanced signal caused by variations in compressibility are amplified by two high electron-mobility transistors and measured at the drain of the second stage, δV_{out}. Carrier density n_{ext} and external field D_{ext} are controlled by top- and bottom-gate d.c. voltages V_{TG} and V_{BG}, in the same way as in the transport measurements.

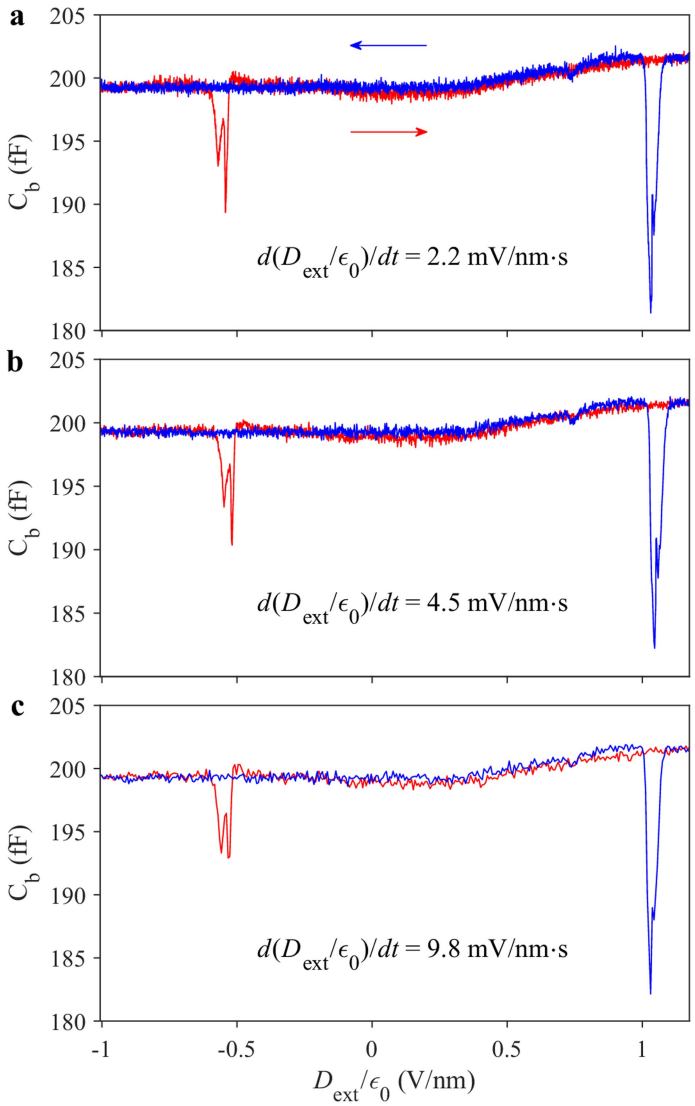

Extended Data Fig. 8 | Independence of the hysteretic behaviour on the sweep rate. a–**c**, Forward (red) and backward (blue) sweeps of the bottom-gate capacitance, C_b, from device H2 at fixed carrier density n_{ext} with sweep rates of 2.2 mV nm^{-1} s^{-1} (**a**), 4.5 mV nm^{-1} s^{-1} (**b**), and 9.8 mV nm^{-1} s^{-1} (**c**). Sweep rates shown in each panel denote the rate at which the externally applied displacement field D_{ext}/ε_0 was ramped in the BN dielectric layers. No noticeable variation was observed in the capacitance features for the large range of sweep rates.

Extended Data Table 1 | Device parameters and characteristics for devices M1, N0, T1 and H1–H4

Device	Bottom BN thickness [nm]	Top BN thickness [nm]	Top-bottom BN relative angle [°]	Protective BN thickness [nm]	Bottom gate material	Top gate material	Geometry	Hysteresis	LSAS
M1	40	40	~ 0	None	Metal	Metal	Hall bar	No	No
N0	42	42	-	20	Metal	MLG	Hall bar	No	No
T1	11	11	-	15	Metal	MLG	Hall bar	No	No
H1	15.5	38	~ 20	8	Metal	Metal	Flower	Weak	No
H2	25	30	~ 30	15	Metal	Metal	Flower	Strong	Yes
H3	28	32	~ 20	5	Metal	Metal	Hall bar	Weak	No
H4	50	50	~ 0	35	Metal	MLG	Hall bar	Strong	Yes

Protective BN means a big BN piece that is used to cover the entire device before fabricating the top gate. The thicknesses of BN were measured by atomic force microscopy. The relative angle between the top and bottom BN is measured using optical second-harmonic generation. For details, refer to Methods. A flower shape means a device geometry as shown in Supplementary Fig. 14.